Chemical screening identifies ATM as a target for alleviating senescence

Hyun Tae Kang[1,5], Joon Tae Park[1,5]*, Kobong Choi[1,5], Yongsub Kim[2], Hyo Jei Claudia Choi[1], Chul Won Jung[1], Young-Sam Lee[3,4]* & Sang Chul Park[3,4]*

Senescence, defined as irreversible cell-cycle arrest, is the main driving force of aging and age-related diseases. Here, we performed high-throughput screening to identify compounds that alleviate senescence and identified the ataxia telangiectasia mutated (ATM) inhibitor KU-60019 as an effective agent. To elucidate the mechanism underlying ATM's role in senescence, we performed a yeast two-hybrid screen and found that ATM interacted with the vacuolar ATPase V_1 subunits ATP6V1E1 and ATP6V1G1. Specifically, ATM decreased E-G dimerization through direct phosphorylation of ATP6V1G1. Attenuation of ATM activity restored the dimerization, thus consequently facilitating assembly of the V_1 and V_0 domains with concomitant reacidification of the lysosome. In turn, this reacidification induced the functional recovery of the lysosome/autophagy system and was coupled with mitochondrial functional recovery and metabolic reprogramming. Together, our data reveal a new mechanism through which senescence is controlled by the lysosomal–mitochondrial axis, whose function is modulated by the fine-tuning of ATM activity.

Cellular senescence has been suggested to be a primary cause of aging and to account for most aging-associated chronic disorders. Hallmarks of senescence encompass changes including permanent cell-cycle arrest, telomere erosion, senescence-associated β-galactosidase (SA-β-gal) activity, and a senescence-associated secretory phenotype[1].

Lysosomes are essential for cellular homeostasis and have many crucial functions including intracellular digestion of macromolecules and organelles. The digestion of endocytosed or autophagocytosed substrates occurs in an acidic compartment whose acidity is maintained by a vacuolar ATPase (V-ATPase) proton pump. V-ATPase is a multisubunit rotary motor composed of two domains: a peripheral V_1 domain responsible for ATP hydrolysis and a membrane-bound V_0 domain responsible for proton translocation[2]. The regulatory mechanism of V-ATPase, achieved through assembly and disassembly of the V_1 and V_0 domains, plays a crucial role in maintaining lysosomal pH[3].

Mitochondria are highly dynamic organelles that undergo continuous fission and fusion cycles. However, dysfunctional mitochondria regularly do not fuse back into the mitochondrial network and instead are eliminated by autophagy, a process through which damaged organelles are degraded[4]. This mitophagy process is crucial for maintaining cellular homeostasis, because dysfunctional mitochondria are incompetent at ATP production but produce more reactive oxygen species (ROS) than do functional mitochondria[5]. Lysosomes and mitochondria are functionally interconnected during senescence[6]. Dysfunctional lysosomes hinder autophagy, thus resulting in accumulation of dysfunctional mitochondria with excessive ROS production[5]. As the major producer of ROS, mitochondria are also the primary target of ROS-induced oxidative damage[7]. This damage in turn further elevates ROS generation, thereby establishing a vicious proaging cycle[6].

In this study, we sought to identify compounds that alleviate senescence, by using high-throughput screening (HTS). This analysis identified the ATM inhibitor KU-60019 as an effective agent.

Because the role of ATM in senescence remains elusive, we performed a yeast two-hybrid screen and identified a new interaction between ATM and the V-ATPase V_1 subunit. Here, we demonstrate that ATM modulates V_1-V_0 assembly in the V-ATPase and regulates senescence via the lysosomal–mitochondrial axis.

RESULTS

Chemical screening for agents that alleviate senescence

The present screening strategy comprised two different methods of measuring the capacity for alleviating senescence: (i) increasing cell numbers and (ii) decreasing SA-β-gal activity. For the primary screen, a DNA-content-based method was used to accurately measure the cell number[8] (**Supplementary Results**, **Supplementary Fig. 1a** and **Supplementary Tables 1** and **2**). A library containing 355 kinase inhibitors was added to senescent fibroblasts, and the effects of these inhibitors on cell proliferation were determined on day 21 (**Supplementary Table 3**). Inhibitors leading to more than a 1.3-fold increase relative to DMSO controls were considered potential hits, and 11 compounds were identified as candidate drugs (**Supplementary Fig. 1b**). A second round of screening was performed to quantitatively measure SA-β-gal activity levels with a chemiluminescence method[9]. Among the 11 drugs, the ATM inhibitor KU-60019 was found to decrease SA-β-gal activity to 30% that of the DMSO control (**Fig. 1a**) and was selected as a candidate agent that may ameliorate the senescence phenotype.

ATM as a potential target to ameliorate senescence

To confirm the proliferation-inducing effect observed in screening, cumulative population doubling (CPD) was measured. Treatment with KU-60019, compared with the DMSO control, increased CPD but did not induce malignant growth (**Fig. 1b** and **Supplementary Fig. 2a**). To confirm the decrease in SA-β-gal activity, SA-β-gal-positive cells were counted. After KU-60019 treatment, the percentage of SA-β-gal positive cells was significantly decreased on day 8, thus suggesting that KU-60019 effectively alleviates replicative

[1]Well-Aging Research Center, Samsung Advanced Institute of Technology, Samsung Electronics, Suwon, Korea. [2]Department of Biomedical Sciences, Asan Medical Center, University of Ulsan College of Medicine, Seoul, Korea. [3]Well Aging Research Center, DGIST, Daegu, Korea. [4]Department of New Biology, DGIST, Daegu, Korea. [5]These authors contributed equally to this work. *e-mail: joontae.park@samsung.com, lee.youngsam@dgist.ac.kr or blueocean2016@dgist.ac.kr
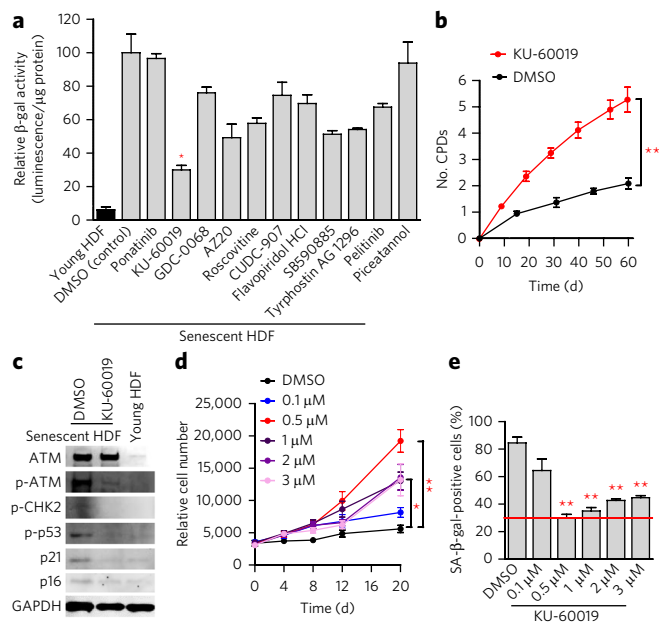
Figure 1 | ATM as a potential target for ameliorating senescence.
(**a**) SA-β-gal activity, measured quantitatively with galacton as the substrate. Means ± s.d., $n = 3$ independent experiments. (**b**) Effects of KU-60019 treatment on the number of CPDs (**$P < 0.01$, one-way analysis of variance (ANOVA) with *post hoc* Tukey's test). Means ± s.d., $n = 3$ independent experiments. (**c**) Specificity of KU-60019 as an ATM inhibitor. GAPDH, loading control. Full gels are shown in **Supplementary Figure 13**. (**d,e**) Optimal strength of ATM attenuation with respect to cell proliferation (**d**) and SA-β gal activity (**e**) (*$P < 0.05$; **$P < 0.01$, one-way ANOVA with *post hoc* Tukey's test). Means ± s.d., $n = 6$ independent experiments.

senescence (**Supplementary Fig. 2b**). We then examined whether KU-60019 could alleviate the stress-induced premature senescence (SIPS) induced by genotoxic stress. Notably, KU-60019 treatment significantly attenuated the etoposide (ETO)-induced senescence phenotype (**Supplementary Fig. 2c**), thus suggesting that KU-60019 allays SIPS as well as replicative senescence.

KU-60019 also decreased the levels of phosphorylated ATM (p-ATM) and its downstream targets (p-CHK2, p-p53, and p21), thus confirming its specificity as an ATM inhibitor (**Fig. 1c**). Furthermore, p16, a senescence-associated marker[10], was decreased after KU-60019 treatment (**Fig. 1c** and **Supplementary Fig. 2d**). Cell proliferation was not induced in senescent ATM-null fibroblasts, thus suggesting that the proliferation-inducing effect of KU-60019 does not arise from an off-target effect (**Supplementary Fig. 2e**). To determine whether directly targeting ATM with short hairpin RNA (shRNA) would yield similar phenotypes to those observed after KU-60019 treatment, senescent cells were transduced with lentiviruses expressing *ATM* shRNA or control shRNA. As the amount of *ATM* shRNA lentivirus increased, the expression levels of ATM and p-ATM decreased in a dose-dependent manner (**Supplementary Fig. 3a**). Regarding KU-60019 treatment, ATM deficiency via *ATM* shRNA decreased SA-β-gal activity and other senescence-associated markers, thus suggesting that this treatment resulted in a phenotype similar to that resulting from KU-60019 treatment (**Supplementary Fig. 3b–f**).

The optimal ATM inhibition level was measured by treatment of senescent fibroblasts with KU-60019 at different concentrations (0–3 μM). The strongest effects in inducing cell proliferation and decreasing SA-β-gal activity were observed after treatment with 0.5 μM KU-60019, and other concentrations (1–3 μM) were less effective (**Fig. 1d,e** and **Supplementary Fig. 3g**). This

result suggested that fine-tuning of ATM signaling may effectively ameliorate senescence phenotypes.

In the screen, the ataxia telangiectasia and Rad3-related protein (ATR) inhibitor (AZ20) was also identified as a candidate compound (**Fig. 1a** and **Supplementary Fig. 1b**). ATR is a member of the PI-3 kinase–related protein kinase (PIKK) family, which includes ATM. To explore the possible involvement of ATR in attenuating the senescence phenotypes, AZ20 as well as the specific ATR inhibitor VE-821 were examined[11]. These inhibitors had no effect on proliferation and did not decrease the percentage of SA-β-gal-positive cells (**Supplementary Fig. 4a,b**), thus suggesting that AZ20 was a false-positive hit in the screening.

ATM interacts with ATP6V1E1 and ATP6V1G1
ATM is a serine/threonine protein kinase that modulates the activity of its interacting partners by phosphorylation[12]. Because the role of ATM in senescence remains elusive, the identification of new interacting partners would provide clues as to ATM's function. Accordingly, we performed a yeast two-hybrid screen with the GAL4 DNA-binding domain (GAL4 BD)-fused human ATM-M domain (residues 811–1466, 656 amino acids (aa)) as bait. We identified 85 positive clones and focused on the V-ATPase V₁ subunits (ATP6V1E1 and ATP6V1G1) because maintaining lysosomal pH via V-ATPase is closely linked to the control of aging[13,14] (**Supplementary Table 4** and **Fig. 2a**). The interaction of ATM-M with ATP6V1E1 and ATP6V1G1 was confirmed with coimmuno-precipitation, which demonstrated that Flag-ATP6V1E1 and Flag-ATP6V1G1 interacted with endogenous ATM (**Fig. 2b**).

We then examined whether ATM directly induced phosphorylation of ATP6V1E1 or ATP6V1G1. Recombinant ATM protein was incubated with recombinant ATP6V1E1 or ATP6V1G1 protein in the presence of ATP. Although both proteins interacted with ATM in yeast two-hybrid and immunoprecipitation assays, only ATP6V1G1 was labeled with ATP, thus suggesting its direct phosphorylation by ATM (**Fig. 2c**); furthermore, in the presence of KU-60019, this phosphorylation was abolished (**Fig. 2c**). Together, these data provide evidence that ATP6V1G1 is an ATM substrate.

ATM controls V₁-domain assembly
During assembly of the V₁ domain, the E and G subunits form a peripheral stator, the E–G heterodimer[15]. Because protein phosphorylation regulates protein-protein interactions[16], we examined the interaction between the E and G subunits. ATP6V1G1 phosphorylation by ATM markedly decreased its interaction with ATP6V1E1, thus indicating that E-G dimerization is directly controlled by ATM *in vitro* (**Fig. 2d**). To validate this result *in vivo*, HEK 293T cells were transfected with Flag-ATP6V1G1. As expected, ATM activation by ETO treatment[17] decreased E-G dimerization *in vivo* (**Fig. 2e**). Because the E–G heterodimer mediates contact with the catalytic hexamer[18], we examined subsequent G1-subunit interactions with the catalytic hexamers (ATP6V1A and ATP6V1B2) and found that ATM activation decreased these interactions (**Fig. 2e**). Notably, the altered interactions recovered after KU-60019 treatment (**Fig. 2e**). Together, these results suggest that ATM regulates V₁-domain assembly.

ATM phosphorylates ATP6V1G1 at Thr77
We next examined the potential ATM-phosphorylation site in ATP6V1G1. The minimal essential motif for an ATM substrate is S*/T*Q (with phosphorylation sites marked with asterisks)[19]. A kinase-prediction tool http://scansite3.mit.edu/, identified a potential phosphorylation motif in ATP6V1G1 at Thr77 (**Supplementary Fig. 5a**). This motif was conserved across species and was similar to that of other ATM substrates including p53, CHK2, and BRCA (**Supplementary Fig. 5b,c**). To validate this prediction, mutation of threonine to alanine (T77A) was introduced in ATP6V1G1 through
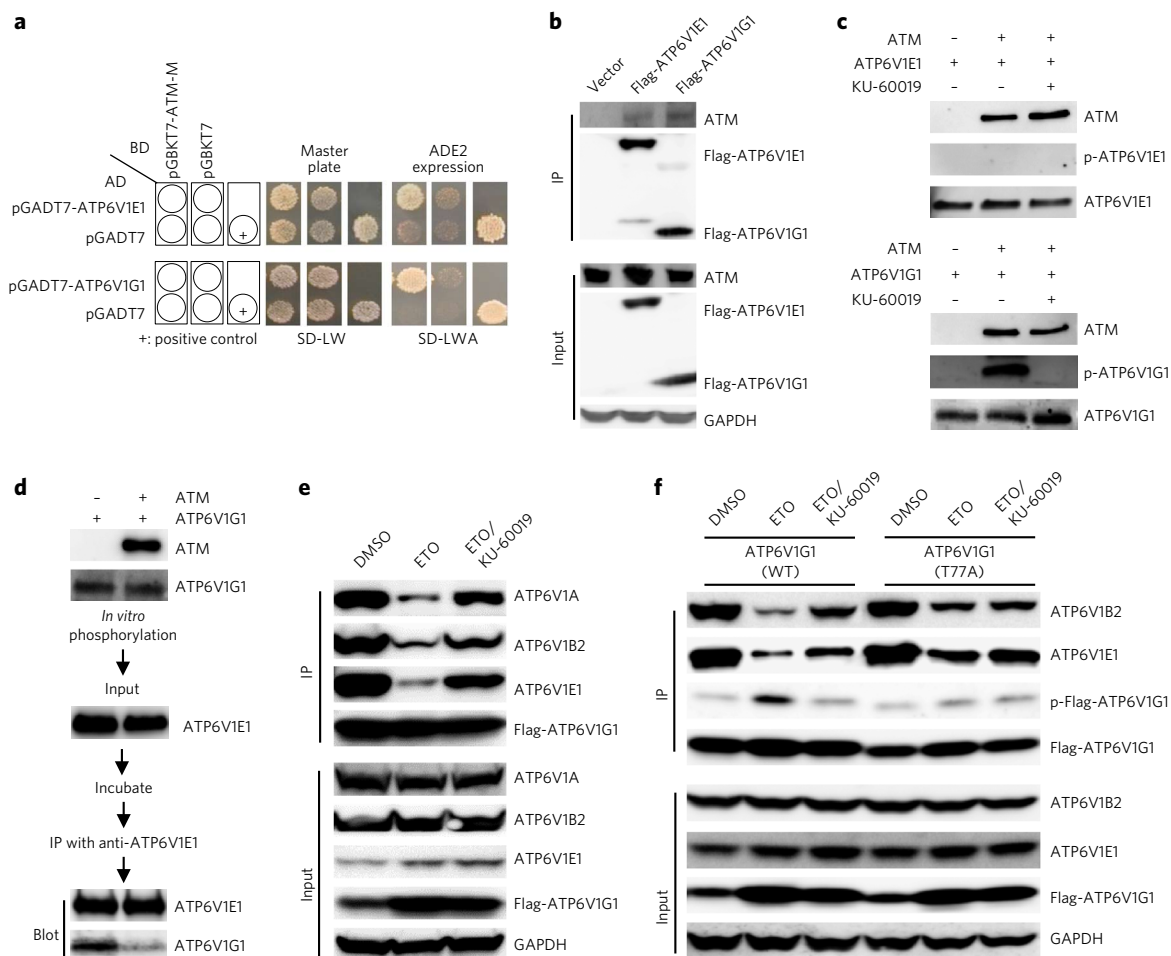
Figure 2 | ATM interacts with ATP6V1E1 and ATP6V1G1. (**a**) The AH109 yeast strain was cotransformed with either the GAL4 BD–fusion plasmid pGBKT7 or pGBKT7-ATM-M. pGADT7-ATP6V1E1 and pGADT7-ATP6V1G1 clones were selected for further study among 85 positive clones. SD-LW, synthetic defined (SD) medium lacking leucine and tryptophan (−LW); SD-LWA, SD medium lacking leucine, tryptophan and adenine (−LWA). (**b**) ATP6V1E1 and ATP6V1G1 coimmunoprecipitation with endogenous ATM. Full gels are shown in **Supplementary Figure 13**. (**c**) *In vitro* phosphorylation of ATP6V1G1 by ATM. Full gels are shown in **Supplementary Figure 13**. (**d**) Effect of ATM on E-G dimerization *in vitro*. Full gels are shown in **Supplementary Figure 13**. (**e**) Effect of ATM on E-G dimerization *in vivo* and subsequent interactions between ATP6V1G1 and catalytic hexamers (ATP6V1A and ATP6V1B2). Full gels are shown in **Supplementary Figure 14**. (**f**) ATM phosphorylation of ATP6V1G1 at Thr77. Full gels are shown in **Supplementary Figure 14**. IP, immunoprecipitate; GAPDH, loading control.

site-directed mutagenesis. ATP6V1G1 (wild type (WT)) phosphorylation was detected by an antibody to pan-phospho-(S/T) ATM substrate; its immunoreactivity was increased by ETO treatment but was blocked by KU-60019 cotreatment (**Fig. 2f**). However, mutant ATP6V1G1 (T77A) phosphorylation was not increased by ETO treatment, thereby suggesting that ATM phosphorylates ATP6V1G1 at Thr77 (**Fig. 2f**).

We then assessed whether ATP6V1G1 Thr77 phosphorylation is critical for regulation of V_1-domain assembly. ATP6V1G1 (WT) and E-subunit interaction was decreased by ETO treatment but was restored by KU-60019 cotreatment (**Fig. 2f**). ATP6V1G1 (WT) and ATP6V1B2 assembly was also decreased by ETO treatment and restored by KU-60019 cotreatment (**Fig. 2f**). However, the ATP6V1G1 (T77A) and E subunit interaction was not affected by ETO treatment, nor was the subsequent interaction of ATP6V1G1 (T77A) with ATP6V1B2 (**Fig. 2f**). Together, these results suggest that ATM regulates V_1-domain assembly through ATP6V1G1 phosphorylation at Thr77.

Finally, we examined the effects of ATP6V1G1 (T77A) on the senescence phenotypes. To knock down endogenous *ATP6V1G1* expression, senescent cells were transduced with lentivirus particles

expressing ATP6V1G1 shRNA, thus resulting in a significant decrease in endogenous *ATP6V1G1* expression (**Supplementary Fig. 5d**). The cells were then transduced with lentivirus particles expressing Flag-ATP6V1G1 (WT) or Flag-ATP6V1G1 (T77A) (**Supplementary Fig. 5e**). ATP6V1G1 (T77A)-expressing cells exhibited a decreased-senescence phenotype (**Supplementary Fig. 5f**). Furthermore, ATP6V1G1 (WT) but not ATP6V1G1 (T77A)-expressing cells were responsive to KU-60019, thus demonstrating that cells expressing ATP6V1G1 (T77A) were not affected by KU-60019 treatment (**Supplementary Fig. 5f**).

ATM controls lysosomal pH by regulating V_1-V_0 assembly

V-ATPase is a biological rotary motor that mediates lysosomal acidification[2]; thus, we hypothesized that ATM might regulate V-ATPase function. We therefore examined the effect of ATM activation on lysosomal pH. Low levels of ETO (5 and 20 µM) slightly increased p-ATM but did not significantly change the lysosomal pH; however, high levels of ETO (80 µM) markedly increased p-ATM and concomitantly increased lysosomal pH (**Fig. 3a**). Notably, the altered lysosomal pH was reacidified after KU-60019 treatment, thus emphasizing ATM regulation of lysosomal pH (**Fig. 3b**).

We further investigated the mechanism underlying ATM control of lysosomal pH. As a peripheral stator, the E–G heterodimer contacts both the C subunit in the V_1 domain and a subunit in the V_0 domain, thus allowing for V_1-V_0 assembly[20]. Because we had identified an ATM-mediated decrease in E-G dimerization, we hypothesized that ATM might control the lysosomal pH through regulating V_1-V_0 assembly. Therefore, we analyzed the effect of KU-60019 on the association between these domains. As expected for a V_0 domain, ATP6V0D1 was associated with membranes (pellet fraction), regardless of KU-60019 treatment (**Fig. 3c**). In contrast, a major fraction of ATP6V1B2 was detected in the cytosol (supernatant fraction), and a minor fraction was found in membranes (**Fig. 3c**). The pellet/postnuclear supernatant ratio of the ATP6V1B2 subunit in senescent fibroblasts was lower than that in young fibroblasts but was increased by two-fold after KU-60019 treatment (**Fig. 3c**). The increased association of the V_1-V_0 domain was expected to reacidify the lysosomal pH during alleviation of senescence; we observed that the lysosomal pH was reacidified on day 8 after KU-60019 treatment (**Fig. 3d**). Together, these observations suggested that the lysosomal reacidification was induced by increased V_1-V_0 assembly after KU-60019 treatment.

To support the subcellular-fractionation results, we visualized V_1-V_0 assembly. First, we examined whether ATM colocalized with ATP6V1G1. As expected, ATM was present predominantly in the nuclei, and a small fraction was found in the cytoplasm, whereas ATP6V1G1 was pervasive throughout the cytoplasm and nuclei, in agreement with previous observations[21] (**Supplementary Fig. 6a**). Colocalization between ATM and ATP6V1G1 was ubiquitous (**Supplementary Fig. 6a**; white arrows). This result is supported by the previous finding that V-ATPase is ubiquitously present in endomembrane organelles, including lysosomes[22], and is also present in the plasma membranes of certain specialized cells[23]. Second, we examined whether ATM regulates V_1-V_0 assembly. ATP6V0D1 is ubiquitously distributed; however, colocalization between ATP6V0D1 and ATP6V1G1 was rarely observed in senescent fibroblasts, whereas their colocalization was reestablished after KU-60019 treatment (**Supplementary Fig. 6b**; white arrows). Together, these results strongly support that ATM regulates V_1-V_0 assembly.

Functional recovery of the lysosome/autophagy system

The maintenance of acidic pH via a V-ATPase is a key mechanism regulating lysosomal function. It provides an optimal environment for lysosomal enzymes to function properly[24] and facilitates autophagic flux[25]; thus, we hypothesized that the reacidification of lysosomal pH would restore the lysosome/autophagy system, which is impaired during senescence[26]. The lysosomal mass and the activity of lysosomal enzymes were examined after KU-60019 treatment. Along with the decrease in lysosomal mass, the activities of cathepsins increased on day 8, thus suggesting the functional recovery of lysosomes (**Supplementary Fig. 7a–d**). Next, the autophagic flux was measured with DQ Red BSA and Cyto-ID[27,28]. After KU-60019 treatment, the autophagic flux increased on day 8, thereby suggesting the functional recovery of autophagy (**Supplementary Fig. 7e,f**). Together, these data suggested that lysosomal reacidification after KU-60019 treatment restored the impaired lysosome/autophagy system by increasing the activity of lysosomal enzymes and enhancing autophagic flux.

Removal of dysfunctional mitochondria through mitophagy

The lysosome/autophagy system is a crucial pathway for the degradation of dysfunctional mitochondria[29]; therefore, we tested whether the recovered lysosome/autophagy system would allow for the removal of dysfunctional mitochondria. The mitochondrial morphology of senescent fibroblasts was more branched and elongated than that of young fibroblasts (**Supplementary Fig. 8a**). Colocalization between mitochondria and the autophagosome
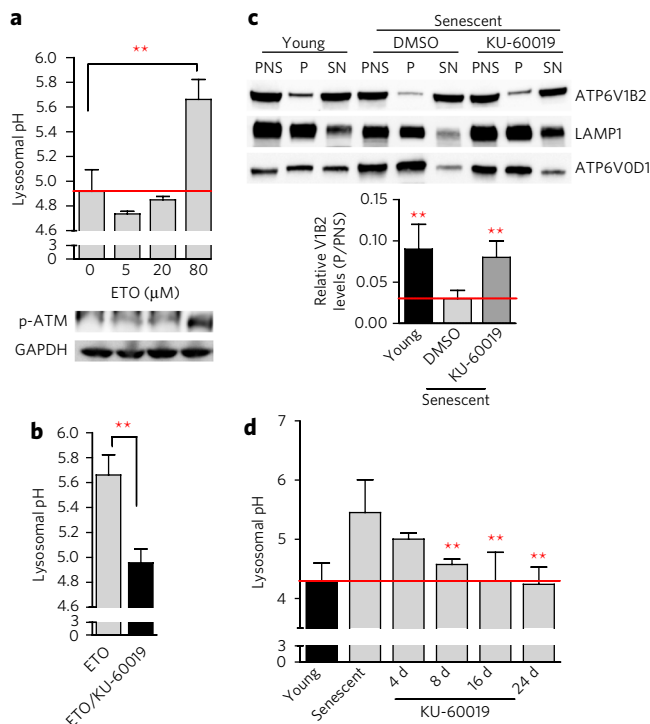
Figure 3 | ATM controls V_1-V_0 assembly in the V-ATPase. (**a**) Flow cytometric analysis of lysosomal pH after treatment with ETO at various concentrations (**$P < 0.01$, one-way ANOVA with *post hoc* Tukey's test). Means ± s.d., $n = 3$ independent experiments. Full gels are shown in **Supplementary Figure 15**. (**b**) Flow cytometric analysis of lysosomal pH after cotreatment with KU-60019 (**$P < 0.01$, one-way ANOVA with *post hoc* Tukey's test). Means ± s.d., $n = 3$ independent experiments. (**c**) Western blots detecting the indicated proteins in postnuclear supernatant (PNS), membranes (P), and cytosol (supernatant (SN)) fractions. The graph shows P/PNS ratios of the ATP6V1B2 intensity normalized to the ATP6V0D1 intensity. (**$P < 0.01$, one-way ANOVA with *post hoc* Tukey's test). Means ± s.d., $n = 3$ independent experiments. Lysosomal-associated membrane protein 1 (LAMP1), lysosomal fractionation control. Full gels are shown in **Supplementary Figure 15**. (**d**) Altered lysosomal pH reacidification after KU-60019 treatment (**$P < 0.01$, one-way ANOVA with *post hoc* Tukey's test). Means ± s.d., $n = 3$ independent experiments.

marker LC3B was observed in young fibroblasts but rarely in senescent fibroblasts (**Supplementary Fig. 8a**; white arrows). After KU-60019 treatment, a young-fibroblast-like mitochondrial morphology was restored, and LC3B colocalization reappeared (**Supplementary Fig. 8a**; white arrows). Additionally, the mitochondrial mass was decreased on day 8, thus suggesting mitophagy activation (**Supplementary Fig. 8b**). To confirm that the recovered lysosome/autophagy system induced mitophagy, we cotreated cells with chloroquine (CQ), which inhibits autophagic flux through the disruption of lysosomal pH[30]. As expected, CQ cotreatment increased autophagosome accumulation (LC3B, green) and colocalization with mitochondria in KU-60019-treated senescent fibroblasts but not in DMSO-treated controls (**Supplementary Fig. 8c**, white arrow). These data suggested that the induction of mitophagy was achieved via the recovered lysosome/autophagy system.

Functional recovery of mitochondria and metabolism

The effective removal of dysfunctional mitochondria by mitophagy is a key mechanism maintaining mitochondrial function[31]; thus, we examined the recovery of mitochondrial function. To evaluate
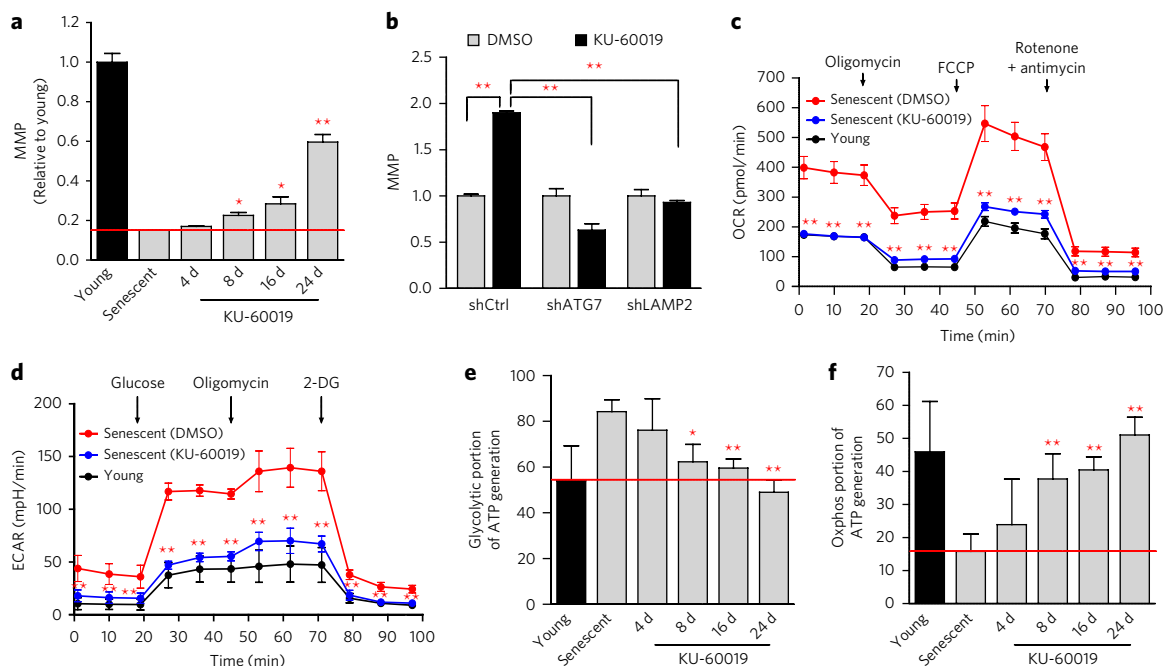
Figure 4 | Recovery of mitochondrial function through activation of the lysosome/autophagy system. (**a**,**b**) Flow cytometric analysis of mitochondrial membrane potential (MMP) with JC-1. MMP change after KU-60019 treatment in senescent cells (**a**) and in senescent cells knocked down *ATG7* or *LAMP2* expression (**b**). (*$P < 0.05$; **$P < 0.01$, one-way ANOVA with *post hoc* Tukey's test.) Means ± s.d., $n = 3$ independent experiments. sh, shRNA; ctrl, control. (**c**,**d**) Measurement of oxygen consumption (**c**) and extracellular acidification rates (**d**) (black line, young fibroblasts; blue line, KU-60019-treated senescent fibroblasts; red line, DMSO-treated senescent fibroblasts) 2-DG, 2-deoxy-D-glucose. (**$P < 0.01$, one-way ANOVA with *post hoc* Tukey's test). Means ± s.d., $n = 3$ independent experiments. (**e**,**f**) Glycolytic (**e**) and oxphos (**f**) portion of ATP generation (*$P < 0.05$; **$P < 0.01$, one-way ANOVA with *post hoc* Tukey's test). Means ± s.d., $n = 3$ independent experiments.

mitochondrial functional status, mitochondrial membrane potential (MMP) was monitored. After KU-60019 treatment, the MMP recovered on day 8 (**Fig. 4a**). To determine whether the recovery of the lysosome/autophagy system was essential for the recovery of mitochondrial function, MMP and mitochondrial mass were measured after shRNA-mediated knockdown of *ATG7* or *LAMP2*, which are essential for autophagosome formation or autophagosome/lysosome, respectively[32]. The impairment of this system prevented the functional recovery of mitochondria (**Fig. 4b** and **Supplementary Fig. 9a**). Furthermore, senescent cells lacking *ATG7* or *LAMP2* did not respond to KU-60019, as shown by a failure to decrease SA-β-gal-positive cells (**Supplementary Fig. 9b**). Together, these data suggested that the autophagic degradation of dysfunctional mitochondria is a prerequisite for senescence amelioration.

To further assess recovery of mitochondrial function, mitochondrial metabolism was examined. The oxygen consumption rate (OCR) and extracellular acidification rate (ECAR) were measured as indicators of oxidative phosphorylation (oxphos) and glycolysis, respectively. The observed rates for senescent fibroblasts were higher than those for young fibroblasts, thus suggesting that senescent fibroblasts consumed more oxygen and showed a greater dependency on glycolysis to meet energy demands, whereas the rates were restored to those of young fibroblasts after KU-60019 treatment (**Fig. 4c,d**). To confirm these results, the proportions of ATP generation from glycolysis and oxphos were compared. The glycolytic part of ATP generation was decreased, but the oxphos part was increased on day 8, thus suggesting that mitochondrial metabolic reprogramming from glycolysis to oxphos was induced after KU-60019 treatment (**Fig. 4e,f**). To determine whether the recovered mitochondrial function affected the alleviation of the senescence phenotype, we cotreated cells with an aconitase inhibitor (deferiprone (DFP))[33]. DFP treatment prevented the KU-60019-induced recovery of mitochondrial

function, through decreasing MMP and shifting mitochondrial metabolism from oxphos to glycolysis, and blocked the KU-60019-induced decrease in the senescence phenotype (**Supplementary Fig. 9c–g**). These data suggested that mitochondrial metabolic reprogramming after KU-60019 treatment is a prerequisite for senescence attenuation.

Decrease in ROS levels and abnormal nuclear morphology
Dysfunctional mitochondria are the major source of excessive ROS production, which causes severe damage in intracellular molecules and cellular organelles[5]; thus, we hypothesized that the recovered mitochondria would generate lower levels of ROS. We measured ROS levels by using two different dyes: DHR123 for hydroxyl radicals and hydrogen peroxides, and MitoSOX for superoxide anions. After KU-60019 treatment, ROS levels decreased on day 4 (**Fig. 5a,b**).

A recent study has shown that the conserved cysteine residues in lamin A, a scaffolding component of the nuclear membrane, are targets of oxidative damage, and their irreversible oxidation induces nuclear disorganization[34]. The decreased ROS levels after KU-60019 treatment led us to conjecture that the frequency of abnormal nuclear morphology might also be decreased. Nuclear morphology was visualized by staining with an antibody to lamin A/C. After KU-60019 treatment, the frequency of abnormal nuclear shapes in senescent cells decreased on day 14 (**Fig. 5c**).

Because ATM is a master regulator of the DNA-damage response[35], ATM inhibition may impair DNA-damage repair, thus consequently leading to DNA-damage accumulation. To exclude this possible adverse effect, we monitored the level of DNA double-strand breaks (DNA DSBs). As previously reported[36], senescent cells exhibited higher DNA DSBs levels than did young cells, whereas KU-60019 treatment did not increase but instead slightly decreased DNA DSB levels (**Supplementary Fig. 10**).
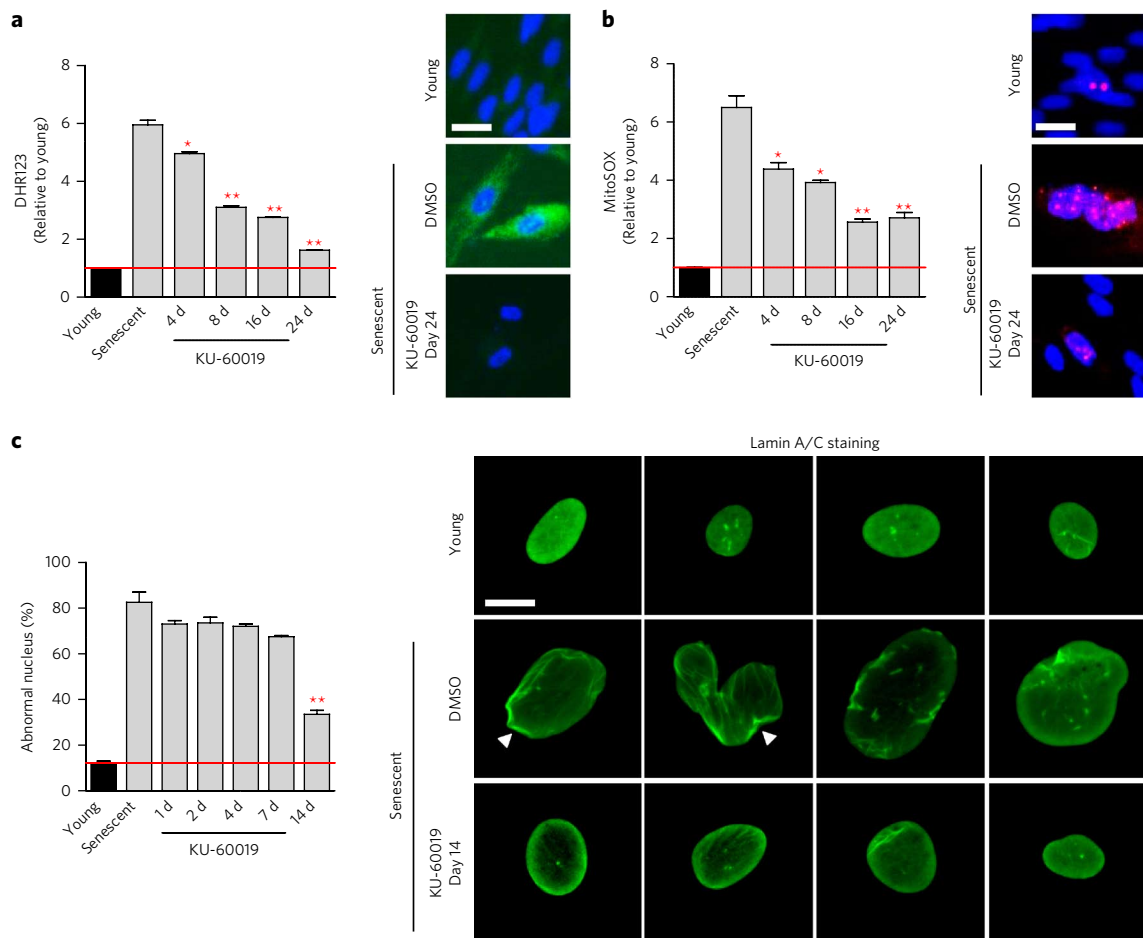
Figure 5 | Decreased ROS levels and abnormal nuclear morphology after KU-60019 treatment. (**a**,**b**) Flow cytometric analysis of mitochondrial ROS with DHR123 (green, DHR123; blue, DAPI nuclear stain) (**a**) and MitoSOX (magenta, MitoSOX; blue, DAPI) (**b**) (*$P < 0.05$; **$P < 0.01$, one-way ANOVA with *post hoc* Tukey's test; scale bar, 10 μm). Means ± s.d., $n = 3$ independent experiments. (**c**) Measurement of abnormal nuclear structures (green, lamin A/C; arrowheads, abnormal nuclear structures; scale bar, 5 μm) (**$P < 0.01$, one-way ANOVA with *post hoc* Tukey's test). Means ± s.d., $n = 100$ stained nuclei per each condition.

Wound-healing-promoting effects of KU-60019

Delayed wound healing in elderly patients decreases quality of life, owing to decreased mobility and increased suffering associated with chronic pain[37]. Therefore, we tested whether KU-60019 treatment might facilitate wound healing in aged mice. Macroscopic analysis of time-matched wounds showed that treatment with KU-60019, compared with DMSO control, markedly accelerated the wound-healing process at early time points (days 3 and 7) (**Supplementary Fig. 11a**). On day 10, wound healing was nearly complete in the KU-60019 group, whereas remnants of scabs were still present in DMSO-treated controls (**Supplementary Fig. 11a**).

To identify the specific mechanism mediating the wound-healing process, immunohistochemical analysis was performed. Sections of excisional wounds were stained with α-smooth muscle actin (α-SMA), a marker of contractile myofibroblasts. α-SMA staining in DMSO-treated controls was dense in the overall granulation tissue, thereby indicating an incomplete resolution of fibrosis. However, staining in the KU-60019 group was diffuse in the dermis area, correlating with the concomitant appearance of collagen fibers, and was strong in the epidermis, correlating with the migration of myofibroblasts to the epidermal region (**Fig. 6a**). Additionally, Masson's trichrome staining revealed that the gross collagen bundling patterns in the KU-60019 group were strong in the overall dermis area and correlated with the maturation/remodeling phase of wound healing (**Fig. 6a**). Furthermore, KU-60019 treatment resulted in thicker collagen than

that observed in DMSO-treated controls (**Fig. 6b**). Finally, proliferating cell nuclear antigen (PCNA) staining indicated that DMSO-treated controls showed selective proliferation in granulation tissue, whereas the KU-60019 group showed proliferation in the suprabasal area of the epidermis (**Fig. 6a**). Quantification of PCNA-positive cells in the epidermis revealed that treatment with KU-60019, compared with DMSO control, resulted in more PCNA-positive cells (**Fig. 6c**). Together, these results suggested that KU-60019 treatment accelerted cutaneous wound healing in aged mice.

DISCUSSION

In this study, we found that ATM mediates previously undescribed mechanisms that control senescence through regulating lysosomal acidification. The maintenance of lysosomal pH is closely linked to the control of aging. Lysosomal pH elevation is age dependent, and lysosomes in aged animals exhibit higher pH[38]. The importance of lysosomal acidification in aging has been highlighted by findings that the V-ATPase regulates life span in fruit flies and yeast[13,14]. These findings are further strengthened by results from our study revealing a previously undescribed role of ATM in lysosomal acidification through regulation of V_1-V_0 assembly in the V-ATPase.

Mitochondria play a crucial role in aging and are regarded to be both targets of and contributors to aging[39]. Mitochondrial dysfunction is evident during senescence, but the means by which the
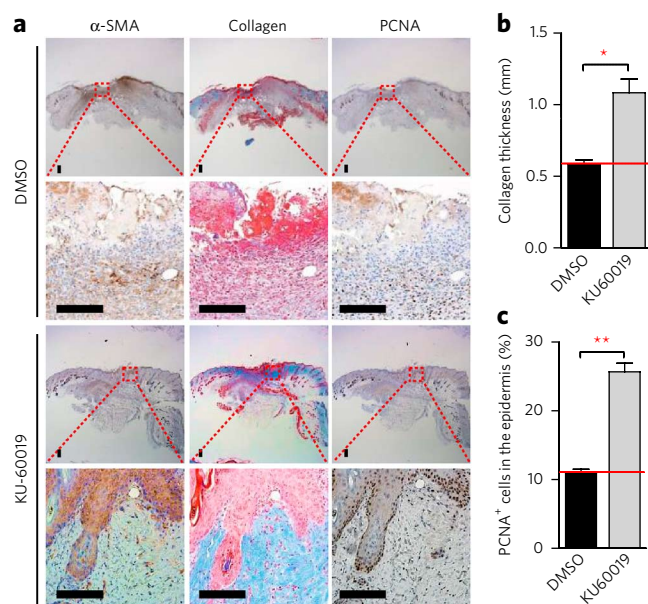
Figure 6 | In vivo effects of KU-60019 on wound healing in aged mice.
(**a**) Immunohistochemical analysis of α-SMA, collagen, and PCNA.
Scale bars, 20 μm. (**b**) Comparison of collagen thickness between DMSO
and KU-60019 groups (*$P < 0.05$, one-way ANOVA with *post hoc* Tukey's
test). Means ± s.d., $n = 3$ individual mouse sections. (**c**) Comparison of
PCNA-positive cells in the epidermis between DMSO and KU-60019
groups (**$P < 0.01$, one-way ANOVA with *post hoc* Tukey's test).
Means ± s.d., $n = 3$ individual mouse sections.

underlying alterations can be delayed or prevented are poorly understood. Here, we discovered a mechanism by which the recovered lysosome/autophagy system leads to the removal of dysfunctional mitochondria through activation of mitophagy and concomitant recovery of mitochondrial function. To our knowledge, no previous reports have described mitochondrial metabolic reprogramming along with the functional recovery of impaired mitochondria. This type of reprogramming is an important criterion to evaluate mitochondrial recovery[40]. We observed that the metabolic shift from glycolysis to oxphos after ATM attenuation is required for restoring senescent phenotypes, thus indicating the necessity of mitochondrial metabolic reprogramming as well as functional recovery in senescence alleviation.

Excessive ROS can cause abnormal nuclear morphology through the oxidation of conserved cysteine residues in lamin A during senescence[34]. We observed a decreased frequency of abnormal nuclear morphology as well as decreased ROS levels. Because the half-life of lamin A is less than 20 h (ref. 41), decreased ROS levels might decrease the oxidative damage in the newly synthesized lamin A and lead to the observed decrease in the frequency of abnormal nuclear morphology. However, it remains possible that the mitochondria might directly affect DNA repair. For example, mitochondria are essential for maturation of Fe–S proteins, which are important for nuclear DNA synthesis and repair[42]. Because uptake of ferrous iron into the mitochondrial matrix strictly requires MMP activation[43], MMP recovery after KU-60019 treatment would also reinitiate iron uptake into the mitochondria and consequently accelerate DNA repair through providing the necessary quantity of mature Fe–S proteins.

ATM belongs to the PIKK family, which includes ATR and DNA-PK[44]. Because these family members share a high level of sequence similarity[44], several approaches to improve ATM-inhibitor specificity have been attempted[45]. Recently, KU-60019 has been shown to inhibit ATM with over 200-fold higher specificity than that of other

PIKKs[46]. Here, ATR inhibitors had no effect toward decreasing senescence phenotypes, thus suggesting that ATM inhibitors may be beneficial for suppressing senescence in cells and organisms, provided that the inhibitor activity is adjusted to a critical level.

ATM has a broad range of putative substrates, which are involved in diverse aspects of cellular physiology, including DNA-damage repair, cell-cycle arrest, and metabolism[47]. To maintain cellular homeostasis, ATM orchestrates the activities of its substrates in response to various stresses[47]. Therefore, for the therapeutic targeting of ATM, ATM activity should be adjusted with sophisticated strategies. The need for this careful approach can be inferred on the basis of evidence that hypomorphic mutations in ATM with various levels of residual kinase activity are associated with mild disease phenotypes in ataxia telangiectasia, whereas null mutations generally exhibit severe disease phenotypes[47]. Accordingly, though we demonstrated that fine-tuning ATM activity via a genetic or chemical approach is beneficial in ameliorating senescence, the potential risk of ATM attenuation remains. Recent studies have revealed that the inhibition of ATM directly causes telomere shortening in human cells, thereby demonstrating its role in the regulation of telomere length[48,49]. Thus, because telomere-length homeostasis is an important factor in aging and aging-associated diseases[50], the therapeutic application of ATM inhibitors should be approached with caution.

In summary, we performed HTS and identified ATM as a potential target for attenuating senescence. We found that ATM controls lysosomal pH through regulating V_1-V_0 assembly in the V-ATPase. Lysosomal reacidification induces functional recovery of the lysosome/autophagy system, which in turn accelerates the removal of dysfunctional mitochondria and results in mitochondrial functional recovery and metabolic reprogramming (**Supplementary Fig. 12**). Together, our results provide evidence that the fine-tuning of ATM activity alleviates senescence and might be clinically applicable to controlling aging and age-related diseases.

METHODS

Methods, including statements of data availability and any associated accession codes and references, are available in the online version of the paper.

References

1. López-Otín, C., Blasco, M.A., Partridge, L., Serrano, M. & Kroemer, G. The hallmarks of aging. *Cell* **153**, 1194–1217 (2013).
2. Forgac, M. Vacuolar ATPases: rotary proton pumps in physiology and pathophysiology. *Nat. Rev. Mol. Cell Biol.* **8**, 917–929 (2007).
3. Kane, P.M. The where, when, and how of organelle acidification by the yeast vacuolar H+-ATPase. *Microbiol. Mol. Biol. Rev.* **70**, 177–191 (2006).
4. Santos, R.X. *et al.* A synergistic dysfunction of mitochondrial fission/fusion dynamics and mitophagy in Alzheimer's disease. *J. Alzheimers Dis.* **20** (Suppl. 2), S401–S412 (2010).
5. Hwang, E.S., Yoon, G. & Kang, H.T. A comparative analysis of the cell biology of senescence and aging. *Cell. Mol. Life Sci.* **66**, 2503–2524 (2009).
6. Kurz, T., Terman, A., Gustafsson, B. & Brunk, U.T. Lysosomes and oxidative stress in aging and apoptosis. *Biochim. Biophys. Acta* **1780**, 1291–1303 (2008).
7. Houtkooper, R.H. *et al.* The metabolic footprint of aging in mice. *Sci. Rep.* **1**, 134 (2011).
8. Silva, L.P. *et al.* Measurement of DNA concentration as a normalization strategy for metabolomic data from adherent cell lines. *Anal. Chem.* **85**, 9536–9542 (2013).
9. Bassaneze, V., Miyakawa, A.A. & Krieger, J.E. Chemiluminescent detection of senescence-associated β galactosidase. *Methods Mol. Biol.* **965**, 157–163 (2013).
10. Campisi, J. Senescent cells, tumor suppression, and organismal aging: good citizens, bad neighbors. *Cell* **120**, 513–522 (2005).
11. Weber, A.M. & Ryan, A.J. ATM and ATR as therapeutic targets in cancer. *Pharmacol. Ther.* **149**, 124–138 (2015).
12. Kurz, E.U. & Lees-Miller, S.P. DNA damage-induced activation of ATM and ATM-dependent signaling pathways. *DNA Repair (Amst.)* **3**, 889–900 (2004).

13. Landis, G.N., Bhole, D. & Tower, J. A search for doxycycline-dependent mutations that increase *Drosophila melanogaster* life span identifies the VhaSFD, Sugar baby, filamin, fwd and Cctl genes. *Genome Biol.* **4**, R8 (2003).

14. Hughes, A.L. & Gottschling, D.E. An early age increase in vacuolar pH limits mitochondrial function and lifespan in yeast. *Nature* **492**, 261–265 (2012).

15. Féthière, J. *et al.* Building the stator of the yeast vacuolar-ATPase: specific interaction between subunits E and G. *J. Biol. Chem.* **279**, 40670–40676 (2004).

16. Tudor, C.O. *et al.* Construction of phosphorylation interaction networks by text mining of full-length articles using the eFIP system. *Database (Oxford)* **2015**, bav020 (2015).

17. Leontieva, O.V. & Blagosklonny, M.V. DNA damaging agents and p53 do not cause senescence in quiescent cells, while consecutive re-activation of mTOR is associated with conversion to senescence. *Aging (Albany, NY)* **2**, 924–935 (2010).

18. Oot, R.A. & Wilkens, S. Subunit interactions at the V_1-V_o interface in yeast vacuolar ATPase. *J. Biol. Chem.* **287**, 13396–13406 (2012).

19. Kim, S.T., Lim, D.S., Canman, C.E. & Kastan, M.B. Substrate specificities and identification of putative substrates of ATM kinase family members. *J. Biol. Chem.* **274**, 37538–37543 (1999).

20. Benlekbir, S., Bueler, S.A. & Rubinstein, J.L. Structure of the vacuolar-type ATPase from *Saccharomyces cerevisiae* at 11-Å resolution. *Nat. Struct. Mol. Biol.* **19**, 1356–1362 (2012).

21. Murata, Y. *et al.* Differential localization of the vacuolar H^+ pump with G subunit isoforms (G1 and G2) in mouse neurons. *J. Biol. Chem.* **277**, 36296–36303 (2002).

22. Nelson, N. & Harvey, W.R. Vacuolar and plasma membrane proton-adenosinetriphosphatases. *Physiol. Rev.* **79**, 361–385 (1999).

23. Wieczorek, H., Brown, D., Grinstein, S., Ehrenfeld, J. & Harvey, W.R. Animal plasma membrane energization by proton-motive V-ATPases. *BioEssays* **21**, 637–648 (1999).

24. DiCiccio, J.E. & Steinberg, B.E. Lysosomal pH and analysis of the counter ion pathways that support acidification. *J. Gen. Physiol.* **137**, 385–390 (2011).

25. Zhou, J. *et al.* Activation of lysosomal function in the course of autophagy via mTORC1 suppression and autophagosome-lysosome fusion. *Cell Res.* **23**, 508–523 (2013).

26. Jung, T., Bader, N. & Grune, T. Lipofuscin: formation, distribution, and metabolic consequences. *Ann. NY Acad. Sci.* **1119**, 97–111 (2007).

27. Vázquez, C.L. & Colombo, M.I. Assays to assess autophagy induction and fusion of autophagic vacuoles with a degradative compartment, using monodansylcadaverine (MDC) and DQ-BSA. *Methods Enzymol.* **452**, 85–95 (2009).

28. Guo, S. *et al.* A rapid and high content assay that measures cyto-ID-stained autophagic compartments and estimates autophagy flux with potential clinical applications. *Autophagy* **11**, 560–572 (2015).

29. Youle, R.J. & Narendra, D.P. Mechanisms of mitophagy. *Nat. Rev. Mol. Cell Biol.* **12**, 9–14 (2011).

30. Shintani, T. & Klionsky, D.J. Autophagy in health and disease: a double-edged sword. *Science* **306**, 990–995 (2004).

31. Cimolai, M.C., Alvarez, S., Bode, C. & Bugger, H. Mitochondrial mechanisms in septic cardiomyopathy. *Int. J. Mol. Sci.* **16**, 17763–17778 (2015).

32. Levine, B. & Kroemer, G. Autophagy in the pathogenesis of disease. *Cell* **132**, 27–42 (2008).

33. Goncalves, S., Paupe, V., Dassa, E.P. & Rustin, P. Deferiprone targets aconitase: implication for Friedreich's ataxia treatment. *BMC Neurol.* **8**, 20 (2008).

34. Pekovic, V. *et al.* Conserved cysteine residues in the mammalian lamin A tail are essential for cellular responses to ROS generation. *Aging Cell* **10**, 1067–1079 (2011).

35. Shiloh, Y. The ATM-mediated DNA-damage response: taking shape. *Trends Biochem. Sci.* **31**, 402–410 (2006).

36. Nassour, J. *et al.* Defective DNA single-strand break repair is responsible for senescence and neoplastic escape of epithelial cells. *Nat. Commun.* **7**, 10399 (2016).

37. Ashcroft, G.S., Mills, S.J. & Ashworth, J.J. Ageing and wound healing. *Biogerontology* **3**, 337–345 (2002).

38. Liu, J. *et al.* Restoration of lysosomal pH in RPE cells from cultured human and ABCA4$^{-/-}$ mice: pharmacologic approaches and functional recovery. *Invest. Ophthalmol. Vis. Sci.* **49**, 772–780 (2008).

39. Brand, M.D. The role of mitochondria in longevity and healthspan. *Longev. Healthspan* **3**, 7 (2014).

40. Brand, M.D. & Nicholls, D.G. Assessing mitochondrial dysfunction in cells. *Biochem. J.* **435**, 297–312 (2011).

41. Cao, K. *et al.* Rapamycin reverses cellular phenotypes and enhances mutant protein clearance in Hutchinson-Gilford progeria syndrome cells. *Sci. Transl. Med.* **3**, 89ra58 (2011).

42. Stehling, O., Wilbrecht, C. & Lill, R. Mitochondrial iron-sulfur protein biogenesis and human disease. *Biochimie* **100**, 61–77 (2014).

43. Breitenbach, M. *et al.* Mitochondria in ageing: there is metabolism beyond the ROS. *FEMS Yeast Res.* **14**, 198–212 (2014).

44. Awasthi, P., Foiani, M. & Kumar, A. ATM and ATR signaling at a glance. *J. Cell Sci.* **128**, 4255–4262 (2015).

45. Hickson, I. *et al.* Identification and characterization of a novel and specific inhibitor of the ataxia-telangiectasia mutated kinase ATM. *Cancer Res.* **64**, 9152–9159 (2004).

46. Golding, S.E. *et al.* Improved ATM kinase inhibitor KU-60019 radiosensitizes glioma cells, compromises insulin, AKT and ERK prosurvival signaling, and inhibits migration and invasion. *Mol. Cancer Ther.* **8**, 2894–2902 (2009).

47. Shiloh, Y. & Lederman, H.M. Ataxia-telangiectasia (A-T): an emerging dimension of premature ageing. *Ageing Res. Rev.* **33**, 76–88 (2017).

48. Lee, S.S., Bohrson, C., Pike, A.M., Wheelan, S.J. & Greider, C.W. ATM kinase is required for telomere elongation in mouse and human cells. *Cell Rep.* **13**, 1623–1632 (2015).

49. Tong, A.S. *et al.* ATM and ATR signaling regulate the recruitment of human telomerase to telomeres. *Cell Rep.* **13**, 1633–1646 (2015).

50. Blackburn, E.H., Epel, E.S. & Lin, J. Human telomere biology: a contributory and interactive factor in aging, disease risks, and protection. *Science* **350**, 1193–1198 (2015).

Author Contributions

H.T.K., J.T.P., and S.C.P. conceived and designed the experiments; H.T.K. elucidated lysosomal pH regulation by ATM and mitochondrial metabolic reprogramming by ATM inhibitor, and performed experiments including *in vitro* phosphorylation, confocal imaging, and flow cytometry detecting lysosomes, mitochondria, and autophagic flux; J.T.P. elucidated the effects of ATM inhibitor by HTS and performed wound-healing experiments and flow cytometry detecting lysosomes and mitochondria; K.C. elucidated the interactions between ATM and the V-ATPase V_1 subunits, and performed subcellular fractionation; Y.K. performed site-directed mutagenesis; H.J.C.C. measured the frequency of abnormal nuclear morphology and performed neutral comet assays; C.W.J. assisted with HTS and wound-healing experiments; Y.-S.L. performed experiments with *ATM* shRNA and ATR inhibitor; H.T.K. and J.T.P. analyzed the data; J.T.P. supervised all experiments; J.T.P., H.T.K., Y.-S.L., and S.C.P. wrote and edited the paper.

Competing financial interests

The authors declare no competing financial interests.

Additional information

Any supplementary information, chemical compound information and source data are available in the online version of the paper. Reprints and permissions information is available online at http://www.nature.com/reprints/index.html. Correspondence and requests for materials should be addressed to J.T.P., Y.-S.L. or S.C.P.

ONLINE METHODS

Cell culture. Human diploid fibroblasts (PCS-201-010; ATCC) and ataxia telangiectasia fibroblasts (ATM-deficient GM02052 fibroblasts; Coriell Cell Repositories) were used in this study. Cells were cultured in Dulbecco's modified Eagle's medium containing 25 mM glucose supplemented with 10% FBS (SH30919.03; Hyclone), 100 U/ml penicillin, and 100 μg/ml streptomycin (SV30079.01; Hyclone). Cells were serially passaged at a 1:4 dilution during early passages and at a 1:2 dilution during late passages. When the population-doubling time (PD) of the cells was more than 14 d and less than 2 d, the cells were considered senescent and young, respectively. Cells were tested for mycoplasma contamination every other week with a Mycoalert mycoplasma-detection kit (LT07-318; Lonza).

Drug screening. Senescent fibroblasts were grown in 96-well plates at a density of 2,000 cells per well. Components of the Kinase Inhibitor Library (L1200; Selleck) were diluted to a final concentration of 0.5 μM and added to the wells every 4 d. At 21 d after drug treatment, cells were washed twice with PBS and lysed in 50 μl of 0.2% SDS. The plates were incubated at 37 °C for 2 h. SYBR Green I (150 μl) nucleic acid gel stain (1:1,000 in distilled water; S-7567; Molecular Probes) was added to the wells. The cell number was determined by measuring fluorescence intensity with a fluorescence microplate reader (Infinite 200 PRO). The mean and s.d. from six replicates were determined for each experimental group.

SA-β-gal staining. SA-β-gal assays were carried out by either a quantitative chemiluminescence assay or X-Gal cytochemical staining. A quantitative chemiluminescence assay was performed with a modified protocol with a Galacto-light System[9]. Briefly, cells were plated in six-well plates. After 2 d, cells were washed twice with PBS and lysed in 50 μl cell culture lysis buffer. Next, 5 μl lysate was incubated with galacton substrate in 200 μl of reaction buffer (20 μM MgCl$_2$ and 100 mM sodium phosphate, pH 6.0) for 40 min at room temperature, and then 300 μl of Emerald Luminescence Amplifier was added immediately before measurement with a luminometer. The values were normalized to the total protein amount in the sample. Bradford assays were used to quantify protein. X-Gal cytochemical staining for SA-β-gal was performed according to the manufacturer's protocol (9860; Cell Signaling Technology).

Colony formation assay. Soft agar assays were performed according to the manufacturer's protocol (ECM570; Millipore). Briefly, 2,500 cells from each condition were plated in six-well plates and incubated for 21 d. Colonies larger than 500 μm in diameter were counted, and representative photographs were acquired for each condition. For anchorage-dependent colony formation assays, 2,500 cells from each condition were plated in six-well plates and incubated for 21 d. Colonies were stained with 0.5% crystal violet solution (HT90132; Sigma).

Western blot analysis. Cells were lysed in Laemmli sample buffer containing 5% β-mercaptoethanol and heated at 100 °C for 5 min. Protein lysates were then separated on 4–12% gradient Tris-glycine mini protein gels (EC60355BOX; Invitrogen) and transferred onto polyvinylidene difluoride (PVDF) membranes (170-4156; Bio-Rad) with a semidry apparatus (Bio-Rad). The membrane was blocked with 5% nonfat dry milk in Tris-buffered saline with 0.1% Tween 20 and incubated with primary antibodies. Subsequently, the membrane was incubated with horseradish peroxidase (HRP)-conjugated secondary antibodies. Proteins were detected with enhanced chemiluminescence solution (32106; Thermo Scientific) with an ImageQuant LAS-4000 digital imaging system (GE Healthcare). The primary antibodies used in this study were rabbit anti-ATM (2873s; 1:1,000 dilution; Cell Signaling Technology), rabbit anti-ATM (phospho-S1981; ab81292; 1:1,000 dilution; Abcam), rabbit anti-phospho-Chk2 (2661; 1:1,000 dilution; Cell Signaling Technology), rabbit anti-phospho-p53 (9284; 1:1,000 dilution; Cell Signaling Technology), goat anti-p21 (SC-397; 1:4,000 dilution; Santa Cruz Biotechnology), mouse anti-p16 (551154; 1:500 dilution; BD Biosciences), mouse anti-GAPDH (G041; 1:1,000 dilution; ABM), mouse anti-Flag (A8592; 1:1,000 dilution; Sigma), rabbit anti-ATP6V1E1 (ab111733; 1:1,000 dilution; Abcam), mouse anti-ATP6V1G1 (SC-25333; 1:500 dilution; Santa Cruz Biotechnology), rabbit anti-ATP6V1A

(ab137574; 1:1,000 dilution; Abcam), mouse anti-ATP6V1B2 (SC-166045; 1:1,000 dilution; Santa Cruz Biotechnology), rabbit anti-phospho-(Ser/Thr) ATM/ATR substrate (2851; 1:1,000 dilution; Cell Signaling Technology), rabbit anti-ATP6V0D1 (ab202899; 1:1,000 dilution; Abcam), and mouse anti-LAMP1 (SC-20011; 1:1,000 dilution; Santa Cruz Biotechnology). The secondary antibodies used in this study were HRP-conjugated anti-rabbit IgG (sc-2004; 1:4,000 dilution; Santa Cruz Biotechnology) and HRP-conjugated anti-mouse IgG (sc-2302; 1:4,000 dilution; Santa Cruz Biotechnology). Antibody validation is available on the manufacturers' websites.

RNA isolation and qRT–PCR. Cells ($1 × 10^6$) were harvested by trypsinization and washed in PBS, and total cellular RNA was extracted with an miRNeasy Mini Kit (217004; Qiagen) and used to prepare cDNA with a Transcriptor First Strand cDNA Synthesis Kit (04 896 866 001; Roche Diagnostics). PCR was carried out with a LightCycler 480 II detection system (Roche Diagnostics) with LightCycler 480 DNA SYBR Green I Master Mix (04 707 516 001; Roche Diagnostics) or Power SYBR Green PCR Master Mix (4367659; Applied Biosystems). Each sample was run in triplicate. The relative expression of each RNA was normalized to the mean value of 18S rRNA. qRT–PCR was performed with the following primers: 5′-AGTCCCTGCCCTTTGTACACA-3′ (18S rRNA-forward) and 5′-CGATCCGAGGGCCTCACTA-3′ (18S rRNA-reverse); p16-forward (P260189-F; Bioneer) and p16-reverse (P260189-R; Bioneer); 5′-CTTTCTTGAAGGTCAGGGGCT-3′ (ATP6V1G1-forward) and 5′-TTTAA GGCTGGCTGCTGCTT-3′ (ATP6V1G1-reverse); and GAPDH primers (PPH00150F-200; Qiagen).

Yeast two-hybrid screen. Yeast two-hybrid screening was performed with the GAL4 BD–fused ATM-M domain (amino acids 811–1466) as bait and a library containing the human pancreas cDNA-activation domain (AD), as previously described[51].

Plasmid construction. The plasmid p3×Flag-ATP6V1E1 was constructed by inserting a cDNA encoding human ATP6V1E1 (GenBank NM_001039366) into the p3×FLAG-CMV 10 vector (E7658-20UG; Sigma). The plasmid p3×Flag-ATP6V1G1 was constructed by inserting a cDNA encoding human ATP6V1E1 (GenBank NM_004888) into the p3×FLAG-CMV 10 vector (E7658-20UG; Sigma). The ATP6V1G1 (T77A) was constructed with a QuikChange site-directed mutagenesis kit (200521; Stratagene) with plasmid p3×Flag-ATP6V1G1. The following sense and antisense oligonucleotide pairs were used to introduce the T77A mutation: 5′-CTGAAGTGGAGAAGGAGGCCCAGGAGAAGATG AC-3′ and 5′-GTCATCTTCTCCTGGGCCTCCTTCTCCACTTCAG-3′.

In vivo **coimmunoprecipitation.** p3×Flag-ATP6V1E1, p3×Flag-ATP6V1G1, and p3×Flag-ATP6V1G1 (T77A) were transfected into HEK 293T (CRL-11268; ATCC) cells. After 48 h, the cells were lysed with lysis buffer (50 mM Tris-HCl, pH 7.4, 150 mM KCl, 1 mM PMSF, 2 mM benzamidine, 0.05% NP-40, and protease-inhibitor cocktail (04693116001; Roche)) and sonicated with a Branson Sonifier 250. The *in vivo* coimmunoprecipitation assays were performed as previously described[52]. The proteins were separated by 10% SDS–PAGE and analyzed by immunoblotting.

In vitro **phosphorylation of ATP6V1E1 and ATP6V1G1.** For *in vitro* phosphorylation, 250 ng of ATP6V1E1 protein (ab40559; Abcam; residues 1–226, full length) or 500 ng of ATP6V1G1 protein (ab40514; Abcam; residues 1–118, full length) was incubated with 25 ng Flag-tagged ATM protein (14-933; Millipore; residues 1–3056, full length) and 100 μM ATP (10585; Affymetrix) in reaction buffer (25 mM HEPES, pH 8.0, 0.01% Brij-35, 1% glycerol, 0.5 mM DTT, 0.1 mg/ml BSA, 10 mM magnesium acetate, and 3 mM MgCl$_2$), and incubated with or without 0.5 μM KU-60019 for 1 h at 30 °C. Reactions were terminated by addition of 6× SDS–PAGE loading buffer. For *in vitro* heterodimerization of ATP6V1E1 and ATP6V1G1, 1 μg of ATP6V1G1 protein was incubated with 50 ng Flag-tagged ATM protein and 100 μM ATP in the same reaction buffer as that used for *in vitro* phosphorylation, then incubated with or without 0.5 μM KU-60019 for 1 h at 30 °C. For heterodimerization of ATP6V1E1 and ATP6V1G1, each reaction mixture was further incubated with 500 ng of ATP6V1E1 protein for 1 h at 30 °C. The entire reaction mixtures

were immunoprecipitated with 1 μg anti-ATP6V1E1 antibody (ab111733; Abcam). The protein samples were separated by 4–12% gradient Tris-glycine mini protein gels (EC60355BOX; Invitrogen), transferred to PVDF membranes and then incubated with mouse anti-Flag antibody (A8592; 1:1,000 dilution; Sigma), rabbit anti-ATP6V1E1 antibody (ab111733; 1:1,000 dilution; Abcam), mouse anti-ATP6V1G1 antibody (sc-25333; 1:1,000 dilution; Santa Cruz Biotechnology), and rabbit anti-phospho-(Ser/Thr) ATM/ATR substrate antibody (2851; 1:1,000 dilution; Cell Signaling Technology). The secondary antibodies used in this study included HRP-conjugated anti-rabbit IgG (sc-2004; 1:4,000 dilution; Santa Cruz Biotechnology) and HRP-conjugated anti-mouse IgG (sc-2302; 1:4,000 dilution; Santa Cruz Biotechnology). Antibody validation is available on the manufacturers' websites.

Measurement of lysosomal pH. Lysosomal pH was measured as described previously[53], with modifications. Cells were incubated in medium containing 500 μg/ml each of Oregon Green 488-dextran (OG488) (D7171; Life Technologies) and cascade blue-dextran (CB) (D1976, Life Technologies) 2 d before the assay. The pH-sensitive fluorescence from OG488 was measured at excitation 490 nm and emission 525 nm, whereas the pH-insensitive fluorescence from CB was measured at excitation 380 nm and emission 425 nm. The OG488/CB ratio of fluorescence from the samples was converted to pH with a standard curve based on data from cells that were incubated with OG488 and CB. Before analysis, cells were treated with high-K^+ solutions (1 mM $MgCl_2$, 10 mM $CaCl_2$, 20 mM NaCl, 120 mM KCl, 5 mM potassium citrate, and 5 mM HEPES) containing 10 μM nigericin (N7143; Sigma) and 100 nM bafilomycin A1 (B1793; Sigma) over the pH range 4.2–7.2. To measure background autofluorescence, cells were incubated in medium without OG488 and CB.

Subcellular fractionation. Cells were homogenized with a prechilled Dounce homogenizer in detergent-free lysis buffer (20 mM HEPES, pH 7.4, 10 mM KCl, 1.5 mM $MgCl_2$, 1 mM EDTA, 250 mM sucrose, 1 mM DTT, and protease-inhibitor cocktail). The homogenates were centrifuged at 10,000g for 10 min at 4 °C, and pellets were prepared as PNS fractions. Supernatant fractions were collected by ultracentrifugation in a Thermo Scientific Fiberlite F50L-24 × 1.5 rotor at 100,000g for 1 h at 4 °C. The pellets were resuspended in lysis buffer and centrifuged at 100,000g for 1 h to wash remaining soluble fractions. Pellets and supernatants were prepared in equal volumes.

Immunofluorescence. For immunofluorescence, cells plated on Nunc Lab-Tek II Chamber Slides (154526; Thermo Fischer Scientific) were fixed with 4% paraformaldehyde in PBS for 15 min at room temperature and then permeabilized with 0.1% Triton X-100 in PBS for 15 min. Blocking was carried out with 10% FBS in PBS at room temperature for 1 h. Samples were incubated with primary antibodies diluted in 10% FBS in PBS overnight at 4 °C. After incubation with rabbit anti-LC3B antibody (2775; 1:1,000 dilution; Cell Signaling Technology), mouse anti-mitochondria antibody (MS601; 1:1,000 dilution; MitoSciences), mouse anti-lamin A/C antibody (MAB3211; 1:1,000 dilution; Millipore), mouse anti-ATM antibody (ab78; 1:100 dilution, Abcam), rabbit anti-ATP6V1G1 antibody (SC-20948; 1:100 dilution; Santa Cruz Biotechnology), or mouse anti-ATP6V0D1 (ab56441; 1:1,000 dilution; Abcam), the cells were washed with ice-cold PBS three times and incubated with Cy3-conjugated anti-mouse antibody (711-585-152; 1:400 dilution; Jackson Labs), Cy3-conjugated anti-rabbit antibody (711-165-152; 1:400 dilution; Jackson Labs), Alexa Fluor 488–conjugated anti-mouse antibody (A-11001; 1:1,000 dilution; Invitrogen), or Alexa Fluor 647–conjugated anti-rabbit antibody (A-21244; 1:1,000 dilution; Invitrogen) for 1 h at room temperature. Antibody validation is available on the manufacturers' websites. The nuclei were then stained with DAPI (R37606; Invitrogen), and samples were mounted with ProLong Gold Antifade reagent (P36934; Invitrogen). Images were captured with a Carl Zeiss LSM 510 confocal microscope.

Measurement of lysosomal mass. Lysosomal masses were measured as described previously[54]. Briefly, cells were incubated with 50 nM LysoTracker Deep Red (L12492; Life Technologies) for 30 min at 37 °C and analyzed on an LSRFortessa instrument.

Measurement of *in vivo* cathepsin activity. Cathepsin activity was determined with MagicRed cathepsin B (CTSB) and cathepsin L (CTSL) assay kits (MR-CTSB and MR-CTSL, respectively; ImmunoChemistry Technologies), according to the manufacturer's instructions. Briefly, cells were incubated in medium containing specific inhibitors for CTSB (20 μM CA-074 Me; Millipore) or CTSL (20 μM CAA0225; Millipore). After 2 h, cells were further incubated with 1× staining solution for 1 h and prepared for fluorescence-activated cell sorting (FACS) analysis. Cathepsin activity was normalized by division of the activity of cathepsins by the lysosomal mass. To calculate the specific activity of cathepsins, the activity of cells with inhibitors was subtracted from the activity of cells without inhibitors. Cathepsin D (CTSD) activity was indirectly measured, as described previously[55]. Briefly, before analysis, cells were incubated in medium containing 4 μM pepstatin A BODIPY FL conjugate (P12271; Life Technologies) and 50 nM LTDR (L12492; Life Technologies) for 30 min. After incubation, cells were prepared for FACS analysis. CTSD activity was normalized to fluorescence from LTDR after subtraction of background autofluorescence.

DQ-BSA assay for analysis of autophagic degradation. Autophagic degradation was monitored with DQ Red BSA (DQ-Red), as described previously[27], with minor modifications. Briefly, cells were incubated with 100 μg/ml DQ-Red (D12051; Life Technologies). This incubation was carried out in complete culture medium, with or without 10 μM chloroquine (CQ) (C6628; Sigma), which was used to block autophagic degradation of endocytosed DQ-Red, for 2 d at 37 °C. At 30 min before the assay, cells were further stained with a Cyto-ID Autophagy Detection Kit (Cyto-ID) (ENZ-51031-K200; Enzo Lifescience) according to the manufacturer's instructions. After staining, cells were prepared for flow cytometric analysis. Fluorescence from DQ-Red was normalized to the fluorescence from Cyto-ID, after subtraction of background autofluorescence. The level of autophagic degradation was calculated by subtraction of the normalized DQ-Red value with CQ from the normalized DQ-Red value without CQ.

Measurement of autophagic flux. Autophagic flux was measured with Cyto-ID as described previously[28], with minor modifications. Briefly, cells were incubated in medium containing 30 μM CQ. At 2 h after incubation, cells were further stained with Cyto-ID staining solution and 50 nM LTDR for 30 min and prepared for FACS analysis. To measure background autofluorescence, cells were incubated in medium without dye. Fluorescence from Cyto-ID was normalized to fluorescence from LTDR. Autophagic flux was calculated with the following equation: ΔMFI Cyto-ID = MFI Cyto-ID (+CQ)/MFI Cyto-ID (−CQ).

Measurement of reactive oxygen species, mitochondrial mass, and mitochondrial membrane potential. For quantification of mitochondrial ROS, the cells were incubated in medium containing 30 μM DHR123 (D632; Life Technologies) and 5 μM MitoSOX (M36008; Life Technologies) for 30 min at 37 °C. For quantification of mitochondrial mass, the cells were incubated in medium containing 50 nM MitoTracker deep red (M22426; Life Technologies) for 30 min at 37 °C. For measurement of the mitochondrial membrane potential, the cells were incubated with 0.6 μg/ml JC-1 (T3168; Life Technologies) for 30 min at 37 °C. After staining, cells were prepared for FACS analysis as previously described[56].

shRNA experiments. For the knockdown of *ATG7* or *LAMP2*, cells were transduced with lentiviruses expressing control shRNA (sc-108080; Santa Cruz Biotechnology), *ATG7* shRNA (sc-41447-V; Santa Cruz Biotechnology), or *LAMP2* shRNA (sc-29390-V; Santa Cruz Biotechnology), as previously described[54]. For the knockdown of *ATM*, *ATM* shRNA constructs were cloned into the pLKO.1-puro lentiviral vector (SHC001; Sigma) with the following oligomers: 5′-CCGGGCAAAGCCCTAGTAACATACTCGAGTATGTTACTA GGGCTTTGCTTTTTG-3′ (forward) and 5′-AATTCAAAAAGCAAAGCCC TAGTAACATACTCGAGTATGTTACTAGGGCTTTGC-3′ (reverse). For the knockdown of *ATP6V1G1*, *ATP6V1G1* shRNA constructs were cloned into the pLKO.1-puro lentiviral vector (SHC001; Sigma) with the following oligomers: 5′-CCGGCAAAGAAGAAGCTCAGGCTGAAACTCGAGTTTCAG CCTGAGCTTCTTCTTTG-3′ (forward) and 5′-CAAAGAAGAAGCTCAGG

CTGAAACTCGAGTTTCAGCCTGAGCTTCTTCTTTGCCGG-3′ (reverse). For lentiviral shRNA production, 293FT human embryonic kidney cells (R700-07; Invitrogen) were transfected with the pLKO.1 lentiviral vector and packaging vectors (VSV-G and PAX2) with Lipofectamine 2000. Viral supernatant was harvested 2 d after transfection and concentrated with Lenti-X (631231; Clontech). Viruses were added to growth medium containing polybrene (6 μg/ml). Stable cell lines were isolated after viral transduction by selection with 2 μg/ml puromycin.

Overexpression of ATP6V1G1 (WT) and ATP6V1G1 (T77A) with the lentiviral system. The PCR fragments of Flag-ATP6V1G1 (WT) and Flag-ATP6V1G1 (T77A) were separately cloned into pLenti6.3 (K5330-00; Invitrogen). 293FT human embryonic kidney cells (R700-07; Invitrogen) were transfected with expression and packaging vectors (VSV-G and PAX2) with Lipofectamine 2000. Viral supernatant was harvested 2 d after transfection and concentrated with Lenti-X (631231; Clontech). Viruses were added to growth medium containing polybrene (6 μg/ml). Stable cell lines were isolated after viral transduction by selection with 5 μg/ml blasticidin.

Seahorse analysis. An XFe24 flux analyzer (Seahorse Bioscience XFe24 Instrument) was used according to the manufacturer's protocol. Briefly, 5×10^4 cells were distributed into each well of an XFe24 cell-culture plate from an XF24 FluxPak (100850-001; Seahorse Bioscience) and then cultured in a 5% CO_2 incubator at a temperature of 37 °C for 16 h. Next, the medium was replaced with XF Assay Medium (102365-100; Seahorse Bioscience), which lacked glucose, and the cells were then cultured for another 1 h in the same incubator. The extracellular acidification rate (ECAR) was measured with an XF Glycolysis Stress Test kit (102194-100; Seahorse Bioscience). The oxygen consumption rate (OCR) was measured with an XF Cell Mito Stress Test Kit (101706-100; Seahorse Bioscience). ECAR was reported in mpH/min, and OCR was reported in pmoles/min. The metabolic shifter aconitase inhibitor deferiprone (379409-5G; Sigma) was used.

Measurement of cellular ATP levels. Cells were incubated in medium with or without 20 μM oligomycin (O4876; Sigma) for 24 h and then lysed with lysis buffer. ATP content was measured with a ViaLight Plus Kit (LT07-221; Lonza) according to the manufacturer's instructions. DNA content was measured with an AccuBlue broad range dsDNA Quantitation Kit (31007; Biotium). For measurements of relative ATP content, the luminescence of each sample was normalized to the DNA content.

Wound healing assay, immunohistochemistry, and trichrome staining. To test whether KU-60019 treatment would promote cutaneous wound healing, five male mice (19-month old; C57BL/6J, Jackson Laboratory) were randomly allocated to each group. Four full-thickness wounds (8 mm in diameter) were created with an 8-mm-diameter biopsy punch on the dorsal surfaces (five mice per experimental group), and 5 μM KU-60019 in 30% Pluronic gel (Pluronic F-127, P2443-1KG; Sigma) was applied to the wounds every day. The wounds were covered with Telfa sponges (Kendall Health Care) after drug application. All animal studies were reviewed and approved by the International Animal Care and Use Committee of the SKKU School of Medicine (SUSM). The SUSM

facility is accredited by the Association for Assessment and Accreditation of Laboratory Animal Care and abides by the Institute for Laboratory Animal Research guidelines. Wounds were measured and photographed each day for 10 d. Immunohistochemistry analyses were performed on paraffin-embedded sections (5 μm) as previously described[57]. The primary antibodies used for immunohistochemistry were mouse anti-α-smooth muscle actin (F3777-2ML; 1:500 dilution; Sigma) and mouse anti-PCNA (SC-56; 1:500 dilution; Santa Cruz Biotechnology). The secondary antibodies used for immunohistochemistry were from the EnVision Detection System (K5007; Dako). Antibody validation is available on the manufacturers' websites. Masson's trichrome staining was performed according to the manufacturer's instructions (25088-100; Polysciences). Measurements of wound size, collagen thickness, and PCNA-positive cells were performed in a blinded manner.

Neutral comet assay. Neutral comet assays were performed with a Single Cell Gel Electrophoresis Assay kit (4250-050-K; Trevigen) according to the manufacturer's protocols, with minor modifications. Briefly, 1×10^5 cells were diluted in 0.5 ml ice-cold PBS. A cell suspension (50 μl) was resuspended in 500 μl LMAgarose (4250-050-02; R&D Systems) and rapidly spread on slides. DNA was stained with SYBR Gold (S-11494; Life Technologies), and olive tail moments (expressed in arbitrary units) were calculated by counting 100–200 cells per condition and then were analyzed with Metafer4 software (MetaSystems) according to the manufacturer's instructions.

Statistical analyses. Statistical analyses were performed with a standard statistical software package (SigmaPlot 12.5; Systat Software). One-way ANOVA with *post hoc* Tukey's test was used to determine whether differences were significant. For statistical analysis, we assumed that values of type I error (α) and power ($1 - \beta$) of 0.05 and 0.80, respectively, were statistically adequate. Then, using G*Power 3.1.9.2 software, the effect size and minimal total sample size were calculated, and sample sizes used in all statistical analyses were sufficient to ensure adequate power.

51. Cho, H., Kim, K.M. & Kim, Y.K. Human proline-rich nuclear receptor coregulatory protein 2 mediates an interaction between mRNA surveillance machinery and decapping complex. *Mol. Cell* **33**, 75–86 (2009).
52. Wei, J.-D., Kim, J.-Y., Kim, A.-K., Jang, S.K. & Kim, J.-H. RanBPM protein acts as a negative regulator of BLT2 receptor to attenuate BLT2-mediated cell motility. *J. Biol. Chem.* **288**, 26753–26763 (2013).
53. Haggie, P.M. & Verkman, A.S. Unimpaired lysosomal acidification in respiratory epithelial cells in cystic fibrosis. *J. Biol. Chem.* **284**, 7681–7686 (2009).
54. Kang, H.T., Lee, K.B., Kim, S.Y., Choi, H.R. & Park, S.C. Autophagy impairment induces premature senescence in primary human fibroblasts. *PLoS One* **6**, e23367 (2011).
55. Chen, C.-S., Chen, W.-N.U., Zhou, M., Arttamangkul, S. & Haugland, R.P. Probing the cathepsin D using a BODIPY FL-pepstatin A: applications in fluorescence polarization and microscopy. *J. Biochem. Biophys. Methods* **42**, 137–151 (2000).
56. Kang, H.T. & Hwang, E.S. Nicotinamide enhances mitochondria quality through autophagy activation in human cells. *Aging Cell* **8**, 426–438 (2009).
57. Lin, J.W. *et al.* Differential requirement for ptf1a in endocrine and exocrine lineages of developing zebrafish pancreas. *Dev. Biol.* **270**, 474–486 (2004).